Overdense plasma generation in a compact ion source

G Castro[1,7], D Mascali[1], S Gammino[1], G Torrisi[1], F P Romano[1,2], L Celona[1], C Altana[1,3], C Caliri[1,3], N Gambino[1], D Lanaia[4], R Miracoli[5], L Neri[1] and G Sorbello[1,6]

[1] INFN-LNS, Via S Sofia 62, I-95123 Catania, Italy
[2] CNR-IBAM, Via Biblioteca 4, I-95124 Catania, Italy
[3] Università degli Studi di Catania, Dipartimento di Fisica e Astronomia, Via S Sofia 64, I-95123, Catania, Italy
[4] Alba syncroton, Carrer de la Llum 2-26, E-08290 Cerdanyola del Vallès, Barcelona, Spain
[5] ESS Bilbao, Poligono Ugaldeguren, E-48170, Zamudio, Spain
[6] Università degli Studi di Catania, DIIEI, Italy

E-mail: Castrog@lns.infn.it

Abstract

Electron cyclotron resonance ion sources (ECRIS) are widely used plasma based machines for the production of intense ion beams in science and industry. The performance of modern devices is limited by the presence of the density cut-off, above which electromagnetic (EM) waves sustaining the plasma are reflected. We hereby discuss the systematic data analysis of electrostatic wave generation in an ECR prototype operating at 3.75 GHz–0.1 THz. In particular, electron Bernstein waves (EBW) have been excited. EBW have already been generated in large-scale plasma devices for thermonuclear fusion purposes. In ion sources where $L_c \sim \lambda_{RF}$ (L_c being the plasma chamber size and λ_{RF} the pumping wave wavelength) the EM field assumes a modal behaviour; thus both plasma and EM field self-organize so that no optical-like wave launching is possible (i.e. the cavity effect dominates on the optical path). The collected data, however, supported by 3D full-wave simulations, actually demonstrate that a Budden-type X-B conversion scenario can be established above some critical RF power thresholds, operating in an off-ECR regime. The generation and absorption of the EBW has been demonstrated by the presence of three peculiar signatures: along with the establishment of an overdense plasma, generation of supra-thermal electrons and modification (non-linear broadening) of the EM spectrum measured within the plasma have been observed. At the threshold establishing such a heating regime, the collected data provide evidence for a fast rotation of the electron fluid.

Keywords: plasma physics, overdense plasma, Bernstein waves, x ray diagnostics, langmuir probe diagnostics, magnetized plasma, plasma hole configuration

1. Introduction

Electron cyclotron resonance ion sources (ECRIS) and microwave discharge ion sources (MDIS) are currently the best devices worldwide to feed high-energy accelerators effectively [1]. Plasma is produced by microwaves, typically in the range 2.45–28 GHz. Microwaves are coupled to a cylindrical chamber working as resonant cavity by a suitable system of waveguides, and absorbed therein during the interaction with low pressure (10^{-6}–10^{-3} mbar) gases or vapours. In presence of a magnetostatic field, the electromagnetic wave absorption is particularly efficient at the so-called 'electron cyclotron resonance' (ECR). Most of the parameters of the extracted beam, such as its intensity, emittance and shape in real space, depend in a decisive way on the characteristics of the plasma from which the beam is extracted [2]. Any further development of ECR-type ion sources is thus intrinsically dominated by physical properties of the plasmas. Additional limitations are given by the high-B mode conditions [3]. In plasmas sustained by microwaves, the

[7] Author to whom any correspondence should be addressed.

density increases quadratically with RF frequency but stabilizes around a value below the critical density n_{cutoff}. In the field of controlled nuclear fusion and magnetic confinement, this topic has crucial importance since it limits the fulfilment of the Lawson criterion. This issue is important for ion sources as well, since the extracted current is directly proportional to the plasma density.

An option to overcome this limitation consists in the use of electrostatic (ES) waves, experiencing no cut-offs within the plasma. An ES wave is a rarefaction-compression wave whose electric field is parallel to the wave propagation direction. Typically, ES waves do not suffer any resonance within a plasma; however, electron Bernstein waves (EBWs) [4] can be strongly absorbed by the plasma at cyclotron harmonics [5]. Due to their electrostatic nature, EBWs must be generated inside the plasma from electromagnetic waves.

EBWs have already been generated in large devices for fusion, and the studies have shown that EBW heating could be a valid alternative to the ECR heating. At the WEGA stellarator in Greifswald, for example, EBW heating allowed densities up to 10 $n_{\text{cut-off}}$ to be reached [6, 7].

Overdense plasmas have been generated in the past in small ion sources in off-resonance conditions [see reference [1] for many examples], and EBW have often been considered as the main cause. However, no systematic study of EBW generation and absorption has been carried out.

In the experiments described here, EBWs are generated and absorbed in a small plasma reactor characterized by an axis-symmetric magnetic field, aimed at the generation of beams for accelerators. In our devices, the wavelength of the pumping wave has the same order of magnitude as the plasma chamber dimensions ($\lambda \sim L$). The EM field assumes a modal behaviour (i.e. the plasma chamber works as a resonator) and the nature of the EM-to-ES modal conversion is different from that in fusion devices. One way to enhance the conversion probability is to tune the pumping wave frequency, in order to establish a suitable modal structure in the cavity, able to be converted into an electrostatic wave [7]. Preliminary results have been published in [8, 9].

Although the theoretical treatment inside metallic resonators has not been fully addressed, we will try in the next section to depict the mechanism according to the classical approach based on right (R), left (L), ordinary (O) and extraordinary (X) nomenclature about wave propagation in magnetized plasmas (see also [1]). From this perspective, two different scenarios have been discussed in literature: direct fast X-EBW conversion, and O-slow X-EBW conversion.

1.1. Theoretical background

In a cold magnetized plasma approximation (i.e. $v_\phi \gg v_{th}$), two main wave types propagate: ordinary or extraordinary waves, differing from each other by their polarization.

The wave propagation depends on the electron density n_e, electron temperature T_e and magnetic field strength B_0. However, for a theoretical treatment it is useful to introduce

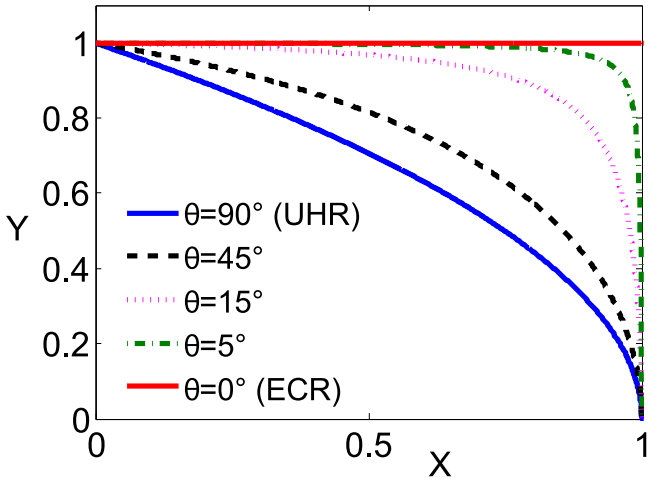

Figure 1. Values of X and Y parameters satisfying resonance conditions of extraordinary wave at propagation angles θ.

the normalized parameters X and Y:

$$X = \frac{\omega_p^2}{\omega_{RF}^2} \propto n_e$$
$$Y = \frac{\omega_c}{\omega_{RF}} \propto B_0 \tag{1}$$

ω_p, ω_c, ω_{RF} being respectively the plasma frequency, the Larmor frequency and the RF frequency.

X and Y are respectively the parametric electron density, proportional to n_e, and the parametric magnetic field, proportional to B_0.

The refraction index $N_{o,x}^2$ of a magnetized plasma can be written as a function of X, Y and the angle θ between the direction of wave propagation and the direction of the magnetic field:

$$N_{o,x}^2 = 1 - \frac{X(1-X)}{2(1-X) - Y^2\sin^2\theta \pm \Gamma} \tag{2}$$

where:

$$\Gamma = \sqrt{Y^4\sin^4\theta + 4Y^2(1-X)^2Y^2\cos^2\theta}. \tag{3}$$

The positive and negative signs in the denominator of equation (2) correspond respectively to the ordinary and extraordinary propagation modes. Resonances occur when the denominator of equation (2) tends to zero, i.e.:

$$\cos^2\theta = \frac{X + Y^2 - 1}{XY^2}. \tag{4}$$

For $\theta = 0°$, a resonance takes place for $Y = 1$, i.e. when $\omega_{RF} = \omega_c$ (the so-called ECR resonance). For $\theta = 90°$, another resonance occurs when $X + Y^2 - 1 = 0$, corresponding to the upper hybrid resonance (UHR):

$$\omega_{RF} = \omega_{UHR} = \sqrt{\omega_c^2 + \omega_p^2}. \tag{5}$$

In a more generalized view, for any value of θ a wave's resonance occurs for a given pair of X and Y. A render view of the resonances, in the X–Y parameter space, is illustrated in figure 1. Although the wave resonance can take place for every

value of θ, just the ECR resonance is able to transfer energy directly from the EM field to the plasma electrons.

This can be easily verified by looking to the solution of the equation of motion for electrons in a collisionless magnetized plasma:

$$\begin{cases} v_x = \dfrac{e}{m_e}\dfrac{-i\omega E_x + \omega_c E_y}{\omega_c^2 - \omega_{RF}^2} \\ v_y = \dfrac{e}{m_e}\dfrac{-i\omega E_y + \omega_c E_x}{\omega_c^2 - \omega_{RF}^2} \\ v_z = \dfrac{e}{m_e}\dfrac{E_z}{\omega_{RF}}. \end{cases} \tag{6}$$

The v_x and v_y components of the electron velocity become infinitely large only when $\omega_{RF} \to \omega_c$.

For propagation angles $\theta \neq 0$, the energy of the EM field can be matched to collective plasma modes. ES waves propagating at 90° with respect to B_0 at harmonics of the cyclotron frequency are called Bernstein waves, having a dispersion relation:

$$1 - \left(\frac{k_b v_{th}}{\omega_p}\right)^2 = e^{-k_b^2 r_L^2} I_0(k_b^2 r_L^2) - 2\left(\frac{\omega_{RF}}{\omega_c}\right)^2 \times \frac{\sum_q e^{-k_b^2 r_L^2} I_q(k_b^2 r_L^2)}{q^2 - \frac{\omega_{RF}^2}{\omega_c^2}} \tag{7}$$

where k_b is wave number of the Bernstein wave, v_{th} the electron thermal velocity, r_L the electron Larmor radius, ω the pumping frequency, I_q is the Bessel function, $q = 1, 2, \ldots, N$.

EBWs are excited at upper hybrid resonance HR via the parametric decay of a large-amplitude electromagnetic wave (frequency ω_0, wave vector $\vec{k}_0$), propagating perpendicular to the ambient magnetic field in the X-mode, into a short-wavelength electron Bernstein wave (frequency ω_1, wave vector $\vec{k}_1$), and a lower hybrid wave or an ion wave (frequency ω_2, wave vector $\vec{k}_2$). The frequencies and wave vectors must satisfy the conditions for the so-called double-resonance [5, 7]:

$$\begin{aligned} \omega_0 &= \omega_1 + \omega_2 \\ \vec{k}_0 &= \vec{k}_1 + \vec{k}_2 \end{aligned} \tag{8}$$

i.e. when both the pumping wave frequency and wavelength approach the frequency and wavelength of the nascent plasma eigenmode. The pump electric fields must overcome a power threshold to allow parametric decay, since the parametric decay instability must be large enough to overcome collisionless and collisional damping [9].

1.2. The excitation of Bernstein waves

Three main mechanisms of EM to EBW coupling have been studied and characterized in plasma fusion devices [12]:

Figure 2 summarizes the three kinds of launching scheme.

1.2.1. High field side launch (arrow 1 in figure 2). X waves are launched by regions where $B_0/B_{ECR} > 1$. X waves are here not screened by the right-hand (R) cut-off, reach the UHR crossing the ECR from the high field side, then being converted into EBWs. Once the density is above the left-hand (L) cut-off, no X-wave propagation is possible anymore. Therefore, the electron density between injection and absorption must stay lower than the L cut-off one. This scheme has been widely implemented in fusion plasma devices, in particular in tokamaks [13] and stellarators [14].

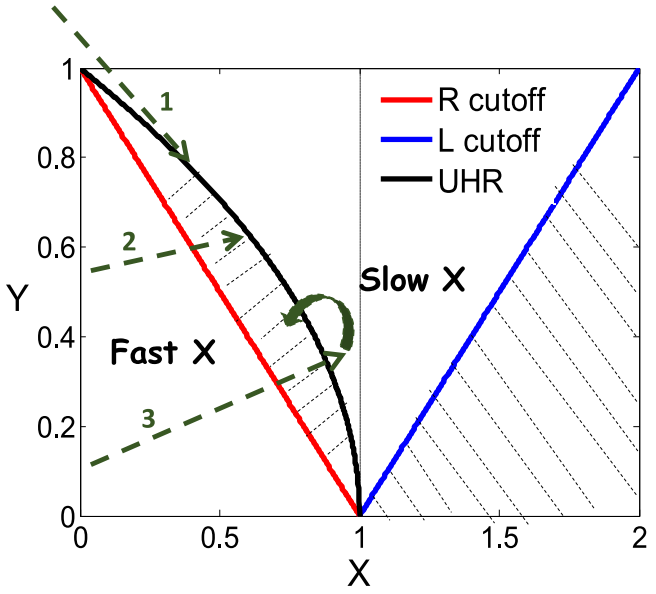

Figure 2. Main mechanism of conversion from the X-wave to the EB waves.

1.2.2. Direct fast X-EBW conversion (arrow 2 in figure 2). The fast X-mode tunnels through the evanescent region between the R-wave cut-off and the UHR, and couples to the slow X-mode (which mode, in turn, converts to EBWs at UHR). Experiments on this mode conversion scheme have been performed at the CDU-X [15] and TST-2 [16] tokamaks and at the MST reversed pinch [17]. If the UHR layer is enclosed by R and L cut-offs, the X wave can be reflected back and forth passing through the UHR. This is the best condition for the establishment of the Budden-type conversion scenario (i.e. a resonator containing mode conversion to EBW as an effective dissipation is formed). The expression of the conversion efficiency of a fast X wave into a Bernstein mode in these conditions is [18]:

$$C_{XB} = 4e^{-\pi\eta}(1 - e^{-\pi\eta})\cos\left(\frac{\phi}{2} + \theta\right) \tag{9}$$

where ϕ represents the phase difference between the slow X-mode propagating towards the L cut-off and the reflected component propagating towards the UHR, η is the Budden [19] parameter—which is obtained by expanding the wave potential around the UHR— and θ is the phase of the gamma function $\Gamma(-i\eta/2)$.

If the length scale of magnetic field variation $L_B = B_0/\frac{\partial B_0}{\partial x}$ is larger than electron density variation length scale $L_n = n_e/\frac{\partial n_e}{\partial x}$, η can be written as:

$$\eta = 294|BL_n|^{UHR}. \tag{10}$$

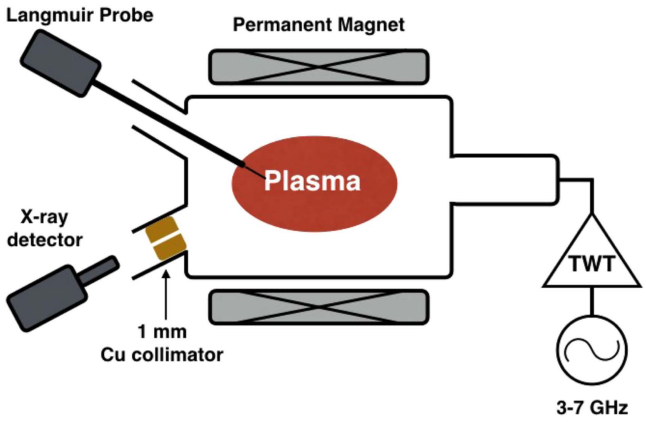

Figure 3. Render view of the plasma reactor and diagnostics used during the measurements.

Direct fast X-EBW conversion heating is used in experiments with relatively low magnetic field, where the normalized gradient length $k_0 L_n$ is ~0.3 (k_0 being the wave number of the incident wave in vacuum) and $\eta \sim 0.22$ [12, 18].

1.2.3. O-slow X-EBW conversion (arrow 3 in figure 2). In such a case, the R cut-off is crossed by the O wave, which, if the conditions for O-slow X conversion are valid at the O cut-off, is converted into slow X waves which are in turn converted into Bernstein waves at upper hybrid resonance. Preinhealter proposed this scheme for the first time in reference [10]; it was then applied at different frequency domains by the Max Planck Institute–IPP group [6, 12].

The efficiency of the O-slow X transition process is given by Mjølhus [9]:

$$\tau_{O-SX} = \exp[-\pi k_0 L_n \sqrt{2Y}(1 + Y)(N_{Z\,opt.} - N_z)^2].$$

τ_{O-SX} is maximized for $k_0 L_n$ of 1–20, i.e. for flattened density profiles.

1.3. Bernstein wave absorption

EBWs exhibit a resonance when the denominator of equation (7) tends to zero i.e. when:

$$B_{res.} = \frac{1}{q} B_{ECR} \quad \mathrm{q} = 1, 2, \ldots, \mathrm{n} \tag{11}$$

corresponding to cyclotron harmonics.

The absorption mechanism of EBW is explained by the Sagdeev–Shapiro damping model [20]. It consists of an acceleration of electrons in the direction perpendicular to the direction propagation across the magnetic field lines. The electrons, trapped by the EBW wave potential, move with the wave and oscillate within the potential well until, at cyclotron harmonics, they acquire sufficient energy to leave the potential well.

The maximum energy reachable by electrons is [5]:

$$W^{\max} = \frac{1}{2} m_e \left(\frac{E_o}{B_0}\right)^2 \tag{12}$$

where E_o is the EBW electric field.

As a result of auto-absorption of the EBWs, Golovanivsky and Dougar-Jabon observed the appearance of shell-like energetic hot electron layers [5] corresponding to sub-harmonics of the cyclotron field. The collisionless damping of the EBW is somehow equivalent to Landau damping for waves propagating perpendicularly to the magnetic field. The absorption coefficient of Bernstein waves depends on electron velocity v. In particular, at the first harmonic ($q = 1$, $B_0 = B_{\mathrm{ECR}}$) the absorption coefficient is proportional to $1/v^3$, while at the second harmonic ($q = 2$, $B_0 = B_{\mathrm{ECR}}/2$), the absorption coefficient is proportional to v. This means that, at the first harmonic, EBW are mainly absorbed by the slower electrons; on the contrary, at the second harmonic, EBW are absorbed more and more by the energetic electrons [12]. This mechanism represents a positive feedback, causing hot electrons to absorb energy from EBW, and thereby to increase further their energy and their capability to absorb EBW.

The same researchers claimed one of the main consequences of the EBW damping was the formation, in case of cylindrical geometry, of an azimuthal electronic current caused by a $\vec{E} \times \vec{B}$ drift. Viscosity and non-linear phenomena could be at the basis of 3D, 'typhoon-shaped' plasmas observed in linear geometries such as the one described in [21].

1.4. Goal of the experiment

Different authors have already shown that plasma density is maximized in the presence of cyclotron harmonics (see [1, 22]), and EBW generation and absorption has been taken into account as one of the possible explanations. However, a complete characterization of the plasma and of the ancillary phenomena related to EBW generation and absorption is missing.

The main goal of the experimental campaign has been the detection of peculiar signatures of ES wave formation and their subsequent absorption, such as:

(1) overcoming the cut-off density;
(2) non-linear heating onset (highlighted by the sudden appearance or increase of x-ray emission above fixed thresholds of RF power);
(3) the appearance of ion signal in the EM spectrum, as a signature of interaction between the EM and ES waves.

While in large size fusion machines the efforts for Bernstein wave generation are going towards O-Fast X-EBW modal conversion, in compact devices the most straightforward mechanism seems to be direct Slow X-EBW conversion, since typical steep density gradients satisfy the relation $k_0 L_n < 1$.

2. Experimental equipment and diagnostics

The plasma reactor (PR) operational scheme is very similar to that of a conventional 2.45 GHz MDIS [23].

The PR consists of a stainless steel cylinder 250 mm long, with a diameter of 136 mm and two welded flanges as

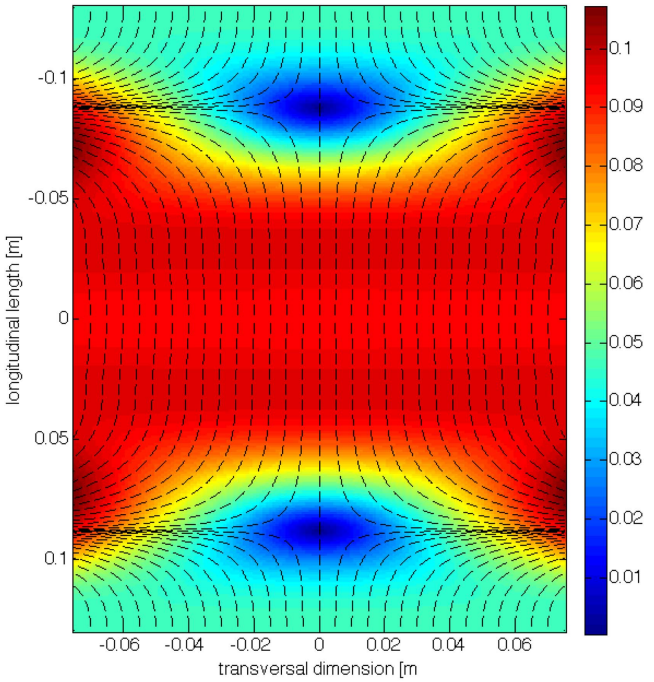

Figure 4. 2D magnetic field of the Plasma reactor and force lines.

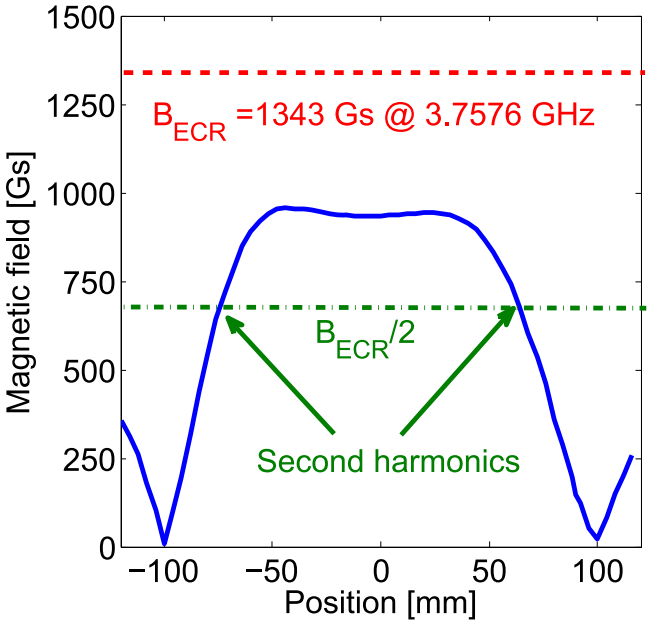

Figure 5. 1D magnetic field of the Plasma reactor along the chamber axis.

endplates of the chamber. Figure 3 shows a render view of the PR, including the several flanges hosting diagnostics tools. A Nd–Fe–B permanent magnets system (radius 75 mm, 180 mm length) generates an off-resonance (above 2.8 GHz) magnetic field along the plasma chamber axis (with a maximum of 0.12 T off axis as shown in figure 4). Because the region of high magnetic field, ∼10 cm long, is smaller than the PR length, there exist some regions where the magnetostatic field drops to zero or flips its sign becoming negative.

The microwaves are generated by a traveling wave tube (TWT) in the frequency range 2–7 GHz, then matched to a WR 187 waveguide through a coaxial cable; a dominant mode TE_{10} is normally excited in the waveguide. Vacuum break is ensured by a window made of a 50 μm thick Kapton sheet. At 2.45 GHz, the magnetic field is suitable to allow ECR ($B_{ECR} = 875$ G) on two different surfaces within the plasma chamber. For microwave frequencies larger than ∼2.8 GHz, the condition $B_0 = B_{ECR}$ is no longer satisfied along the axis.

Hence, for frequencies larger than ∼3 GHz, no direct ECR heating is allowed.

Tests have been carried out at 3.7576 GHz, in order to avoid any chance to have ECR heating. This frequency has been chosen after a fine frequency tuning in order to maximize the plasma density and minimize the reflected power to the TWT. The choice of such a frequency ensures that gas breakdown occurs in off-resonance conditions. However, as shown in figure 5, at 3.7576 GHz, harmonics of ECR exist within the reactor. In these positions, we expect to find eventual signatures of EBWs absorption, in case of their inner-plasma generation.

Plasma has been characterized by means of several diagnostics tools:

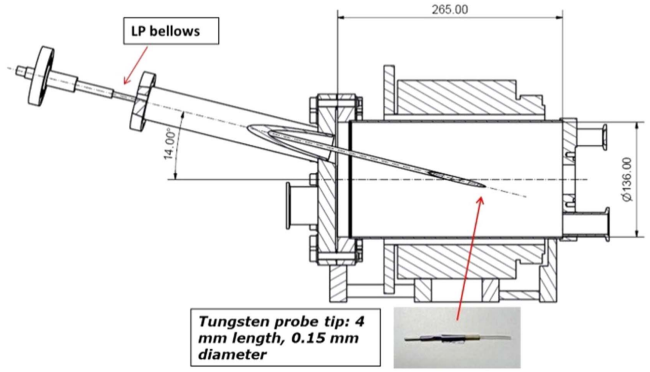

Figure 6. LP apparatus: the LP penetration axis has a 14° inclination w.r.t. the plasma chamber axis.

(1) a movable Langmuir probe;
(2) Si-pin/SDD x-ray detectors;
(3) a full-field x-ray pinhole camera.

Both classes of diagnostics will be described in the following.

2.1. Langmuir probe data analysis

The Langmuir probe used during the measurements consisted of a tungsten tip with a diameter of 0.15 mm and a length of 0.4 mm. The tip, inserted in a tungsten core coated with alumina, is connected to a handling system via a bellows as shown in figure 6. Plasma parameters were obtained by sweeping the probe voltage from −100 V to +100 V with steps of 1 V. Due to the expected high density regime, the resistivity curves were analyzed by means of different models validated in the density range of interest.

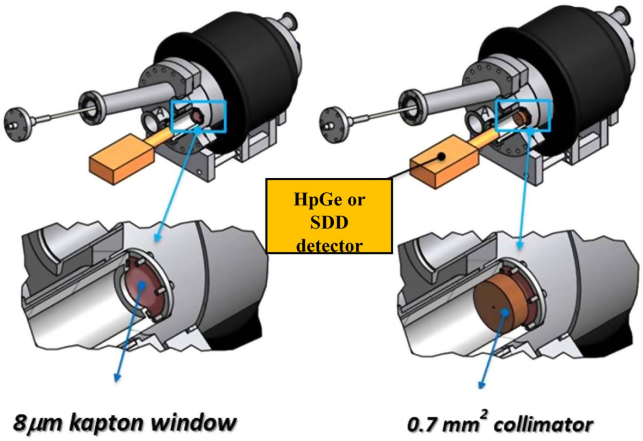

Figure 7. Focus on the kapton layer and 1 mm collimation positioning during experimental measurements carried out with HpGe and SDD detectors.

- The floating potential method (FPM), proposed by Chen, validated in the range $0.5–5 \cdot 10^{11}\,\mathrm{cm}^{-3}$ by comparison with microwave interferometry [24]
- The Allen, Boyd and Reynold model (ABR) [25], neglecting ion orbital motion
- The Bernstein, Rabinowitz and Lafambroise (BRL) model [26, 27], solving the equation of motion as a function of the particle energy and angular momentum.

  Chen has shown that ABR underestimates the plasma density, while BRL overestimates it. However, their geometric mean gives approximately the right density [28]
- Finally, the orbital motion limited (OML) theory has also been used. Although this model fails in the density range $1 \cdot 10^{9}–1 \cdot 10^{10}\,\mathrm{cm}^{-3}$ [29], MW interferometry demonstrates that at higher plasma densities ($n_e > 1 \cdot 10^{11}\,\mathrm{cm}^{-3}$), the OML model could represent a reliable and simple way to derive the plasma parameters [30].

2.2. X-ray diagnostics

The x-ray radiation emitted by the plasma has been detected by means of different devices:

- A high purity germanium (HpGe) semiconductor detector for the detection of x-rays in the range 1–40 keV, (Mod. EGX.30 of the EURYSIS MEASURES), 200 eV resolution.
- A silicon drift detector (SDD), complementary to the first one, able to detect X radiation in the range 2–30 keV. Its energy resolution is 160 eV at the reference line of 5.9 keV, and it is able to operate at high counting rates (up to 500 kcps).

The measurements have been carried out on x-rays emitted from the plasma through an $8\,\mu$m thick Kapton window.

Furthermore, the x-ray beam was collimated by a brass collimator having $\phi = 1$ mm as diameter and 5 mm thickness, as schematically shown in figure 7.

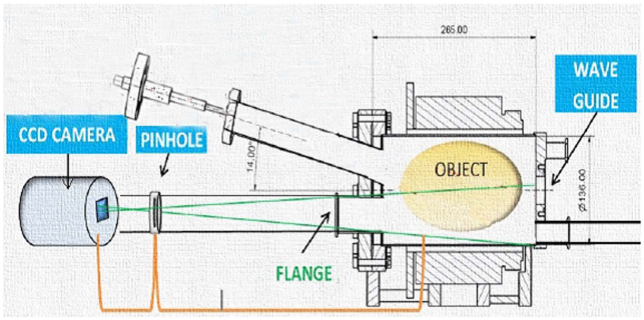

Figure 8. Positioning of the pinhole camera on the plasma reactor.

In a second stage, space resolved x-ray imaging performed by means of an x-ray pinhole camera coupled to a CCD camera has been implemented: the x-ray pinhole camera allows the formation of images through the use of a small circular aperture (pinhole) acting as a lens of infinite focal length for photons having wavelength smaller than 20 nm (~60 eV).

A back-illuminated, electronically cooled CCD camera (ANDOR, IKON Model DO934-M BR-DD [31]) is the 'core device' of this diagnostics tool. It allows space resolved detection of plasma emitted x-rays in the energy range 1–30 keV.

The technique used in this work is to be described in detail in reference [32].

The geometry and the cone of view intercepted by the x-ray pinhole camera (XPC) are shown in the sketch of figure 8.

The x-ray imaging has permitted exploration of, in particular, the structure of the plasma under different heating conditions, highlighting the regions populated by the most energetic electrons.

2.3. Ancillary diagnostics

The EM spectrum within the plasma chamber, with and without the plasma, has been detected by means of the Langmuir probe tip, working as an electromagnetic antenna. The collected signal has been de-convolved and spectrally analyzed by a HP 8565E spectrum analyzer, while a diode power meter has been used for the EM power measurements. Finally, a Gauss-meter has been used to detect any modifications of the magnetic field strength due to the eventual generation of inner-plasma particle fluxes.

3. Experimental results

3.1. X-ray spectroscopy

Volumetric x-ray spectroscopy has been performed to explore the plasma energy content versus the RF power trend. These measurements give a clear and prompt insight of any eventual non-linearity in wave-plasma interaction. We operated in an Ar plasma at $1.5 \cdot 10^{-4}$ mbar. Figure 9 shows the rate of x-rays counted by the detector for different values of RF power. For RF power lower than 45 W, the detector reveals just a few counts; however, with only a few watts more, at

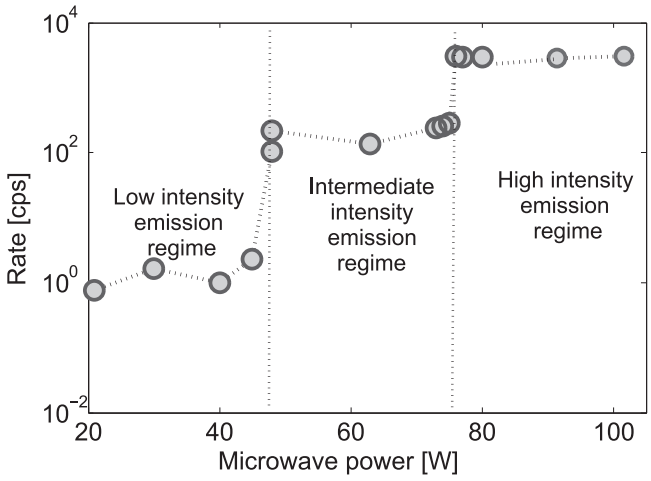

Figure 9. X-ray emission rate versus RF power at $1.5 \cdot 10^{-4}$ mbar. Three different emission regimes exist.

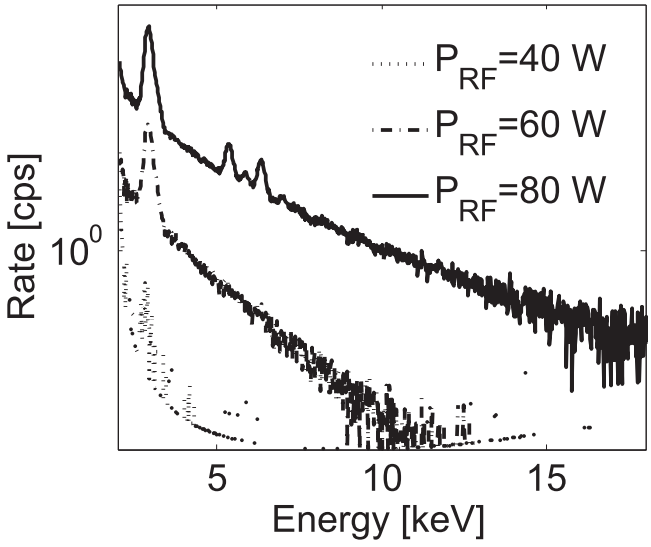

Figure 10. X-ray spectra for different values of the RF power.

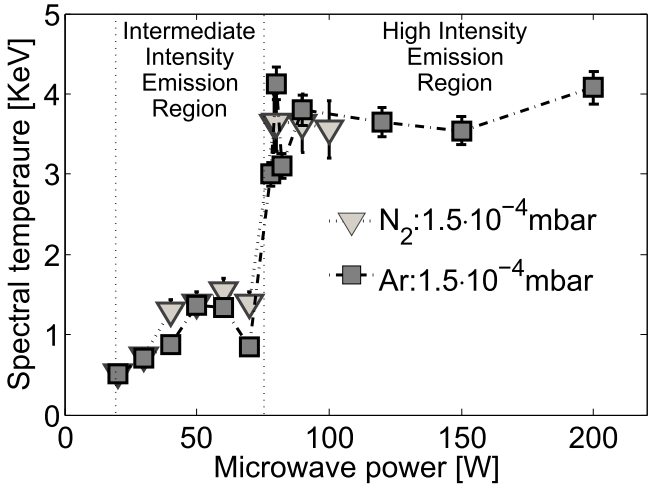

Figure 11. Spectral temperature versus RF power for N_2 and Ar plasma.

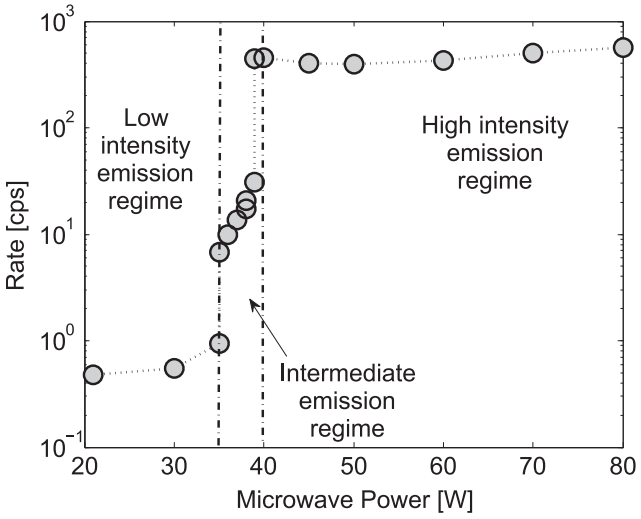

Figure 12. X-ray emission rate versus RF power at $4 \cdot 10^{-4}$ mbar—Ar plasma.

$\sim$46–48 W the rate suddenly increases up to several hundreds of counts s^{-1}. A second power threshold is found at around 78 W, where the emission rate increases by a factor 10, up to $3 \cdot 10^3$ cps. These first rough data are enough to figure out three emission regimes corresponding to three heating regimes of the plasma:

- A **low intensity emission regime** (LIER), below 46 W, characterized by no x-ray emission.
- An **intermediate intensity emission regime** (IIER), for 48 W < RF power < 78 W, characterized by moderate x-ray emission ($\sim 10^2$ cps);
- A **high intensity emission regime** (HIER), for RF power higher than 78 W, characterized by emission rate $>10^3$ cps.

The non-linear boost of the emission rate as each RF power threshold is overcome is dramatic.

Some of the spectra measured during the experimental campaign, and characterization of each emission regime, are shown in figure 10. The lines of the x-ray fluorescence of Argon and of the components of the plasma chamber (steel) are superimposed to the Bremsstrahlung spectrum.

Each emission region is characterized by a different spectral temperature, obtained by the Maxwellian fit of the spectrum [33]. In addition, the spectral temperatures show a 'threshold-like' behaviour, as shown in figure 11. The trend is very similar when operating with a nitrogen plasma at the same pressure. The spectral temperature jumps from $\sim$1 keV in the IIER up to $\sim$4 keV in the HIER.

The value of the power thresholds between the different regimes depends on the background pressure—both increasing with growing pressure.

For example, figure 12 shows the rate of incoming x-rays to the detector versus RF power at the pressure of $4 \cdot 10^{-4}$ mbar. In this case, just 34 W are enough to trigger the intermediate emission regime, and 39 W to trigger the high intensity emission regime.

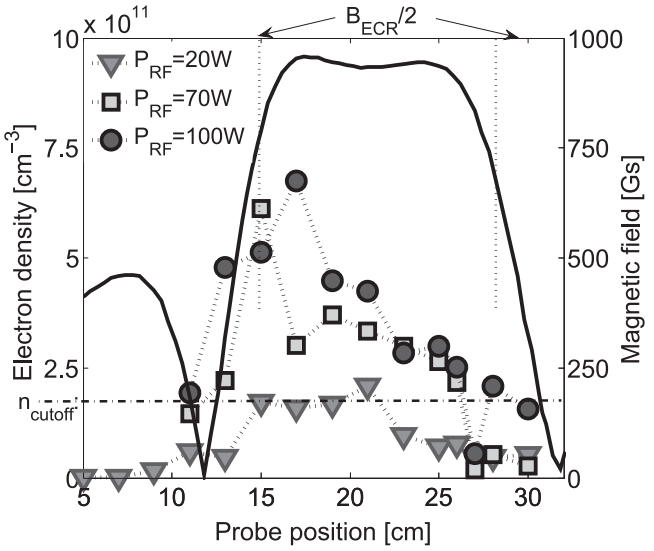

Figure 13. Electron density along the probe penetration axis for different RF power obtained with the FPM method. Density cut-off at 3.7576 GHz ($1.75 \cdot 10^{11}$ cm^{-3}) is also shown.

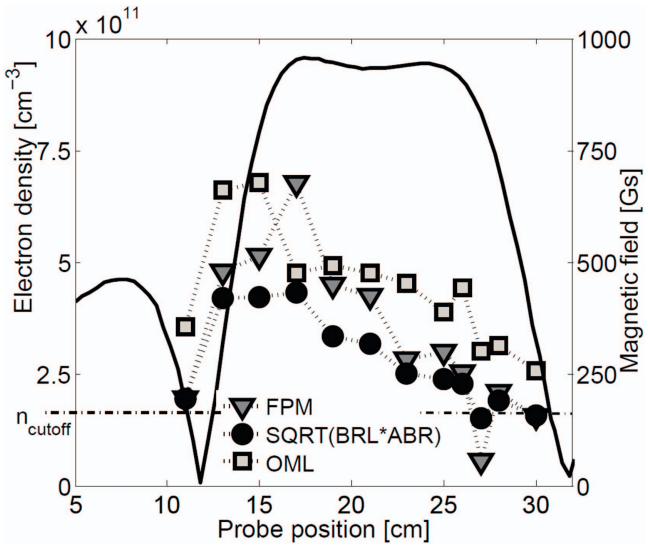

Figure 14. Comparison between normalized densities along the probe penetration axis, obtained with different LP method, at 100 W RF power.

3.2. Langmuir probe measurements

Plasma density and temperature of the cold electrons were measured by means of the above-described Langmuir probe.

Figure 13 shows the value of the normalized electron density X for different values of the RF power along the LP penetration axis. For sake of simplicity, only the values obtained by FPM method have been inserted in the figure 13. At 20 W plasma is still under-dense (i.e $X < 1$) everywhere, meaning that the LIER is indeed related to an under-dense plasma.

With increasing RF power, X becomes >1 (overdense plasma). In particular, at 100 W (corresponding to the high intensity emission regime), up to $7 \cdot 10^{11}$ cm^{-3} electron density is measured, corresponding to a normalized density of $X \sim 4$. At 70 and 100 W, the plasma is overdense everywhere along the LP penetration axis except at position 27 cm. A clear peak in the electron density profile is placed in proximity of the second cyclotron harmonic (around 13–15 cm probe position).

Due to the relevance of the results, the LP data were analyzed with the above-mentioned collection of models. Figure 14 shows the value of the electron density at 100 W of pumping wave power as it comes out from such different models. OML provides the larger density values, while the geometric mean between BRL and ABR methods gives the lowest values. However, they all confirm the overcoming of the cut-off density by a factor varying from 2.3 (geometric mean between BRL and ABR methods) and ~ 4 (OML). Although the electron density measured at 100 W is larger than at 70 W, the variation is very low. Apparently, LP diagnostics is not sensitive to the transition from IIER to HIER. In figure 15, electron temperature is plotted against probe position. Even in this case the maxima of temperature are found around the second harmonic of the cyclotron resonance.

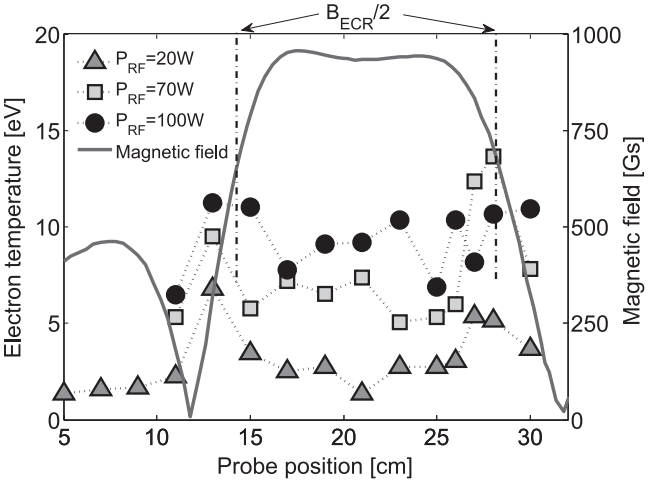

Figure 15. Electron temperature along the probe penetration axis for different RF power.

The formation of the highly overdense plasma and the local peaks of density and temperatures as measured by the LP in proximity of the cyclotron harmonics are already clear signatures that electron Bernstein modes have been internally generated above the critical power threshold.

3.3. Electromagnetic spectral emission analysis

A part of the experimental activities was dedicated to exploring the non-linear interaction of the incoming radiation with the plasma. The non-linear interaction has been deeply studied both in ECRIS [34] and at the W7-AS stellarator [35]. Specific analysis in our set-up has been published elsewhere [36]. In figure 16, the pumping wave spectrum is shown, for varying RF power (the horizontal axis shows the pumping wave frequency). There is a clear difference in such spectra when measured below or above the power threshold—the same difference we found in analysing the x-ray emission. It

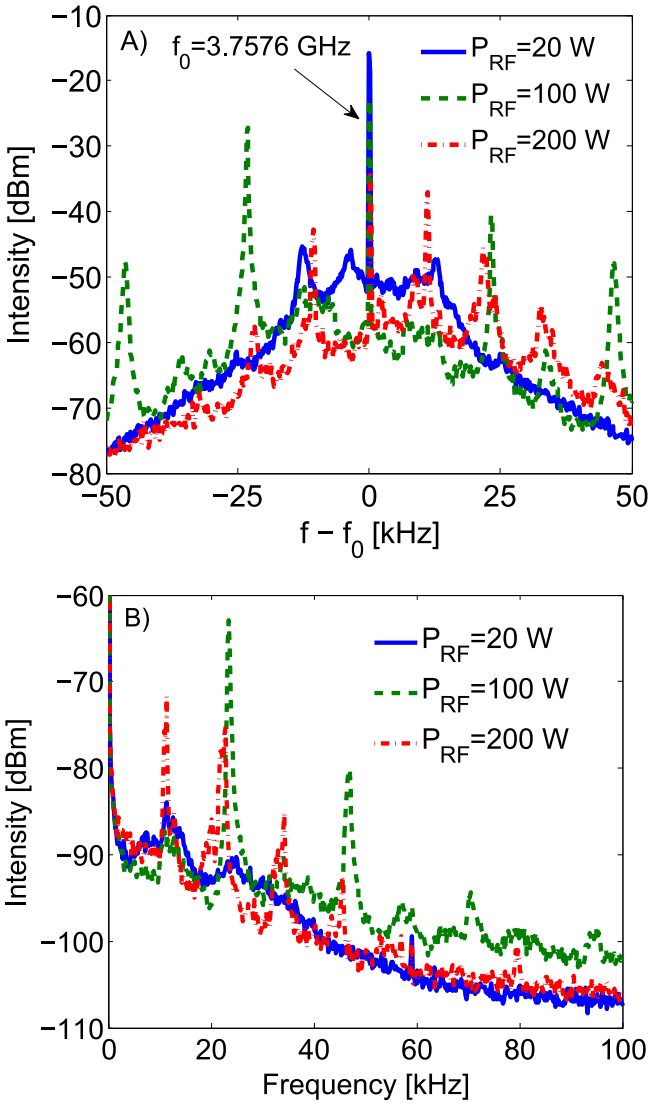

Figure 16. (A) Wave spectrum around the pumping wave at $1.5 \cdot 10^{-4}$ mbar, 60 W RF power, (span 100 kHz, bandwidth 300 Hz). (B) Low frequency spectrum. The space between sidebands equals the signal frequency in the low frequency range.

is interesting to compare the spectral characteristics among the three regimes described in section 3.1, as in the following.

- **LIER**: Below the power threshold of 48 W, the measured EM spectrum contains the pumping wave at 3.7476 GHz only. The spectrum has a FWHM of ∼50 kHz (see figure 17).
- **IIER**: When the power is increased above the first threshold, several 'sidebands' around the pumping wave frequency appear. The sideband frequency gaps Δf vary in the range 7–15 kHz. Δf varies with the background pressure and the magnetic field at the measurement point. The sidebands in the high frequency domain are every time accompanied by waves in the kHz range. The frequency of these low frequency waves correlates closely with Δf.

An example of spectrum around the sidebands and in the KHz range is shown in figure 16. Figure 16(a) shows

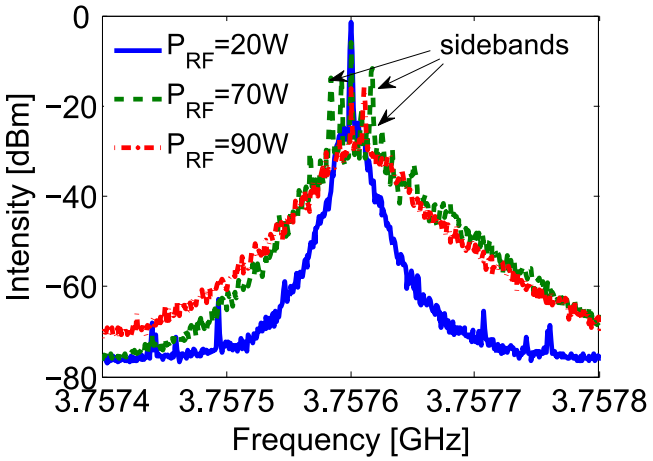

Figure 17. Wave spectrum for increasing RF power at $1.5 \cdot 10^{-4}$ mbar.

the intensity of the signal when moving around the pumping wave f_0 for varying RF power, while figure 16(b) shows the signal in kHz in the same experimental conditions. To every sideband at distance $f - f_0$ from the pumping wave corresponds a wave at frequency $f - f_0$ in the kHz range.

In addition to the 'comb-like' transition of the high frequency spectrum, the spectrum broadens up to FWHM ∼ 100 kHz (see figure 17). Broadening and sidebands appear to be symmetric with respect to the pumping wave, in accordance with a modulation instability mechanism due to the strong non-linear coupling between EM waves and plasma, as described in [34].

- **HIER**: Overcoming the second RF power threshold, the spectrum ultimately changes: the comb-like structure turning into a broad and smooth collection of frequencies (see figure 16). The sidebands in the kHz range are modified in frequency and intensity, while peaks at frequencies hundreds of kHz away from that of the pumping wave appear, together with a relatively high amplitude wave in the MHz range [36] (see figure 18). This new wave at $f \sim 8$ MHz is compatible with Lower Hybrid oscillations.

Data available up to date are not enough to support a unique interpretation. Different decay mechanisms can be taken into account, in particular a decay into lower hybrid waves and Bernstein waves and decay into acoustic-ion waves and Bernstein waves. These mechanisms can also act together as shown in reference [37]. These data support modulation instability onset as well. The spectral properties so far remarked are particularly evident at the 13 cm longitudinal position, corresponding to the second ECR harmonics.

3.4. Plasma structure characterisation by optical and x-ray imaging

The plasma structure in the different heating regimes was explored by means of optical and x-ray inspection. In both

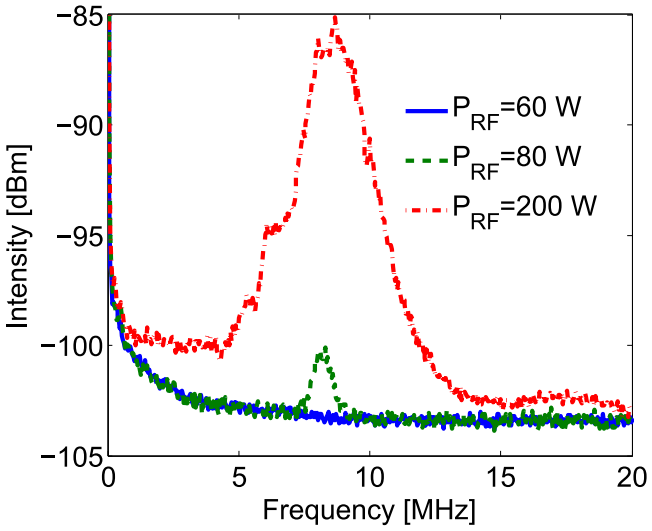

Figure 18. Low Frequency Spectra collected at different pumping wave frequencies.

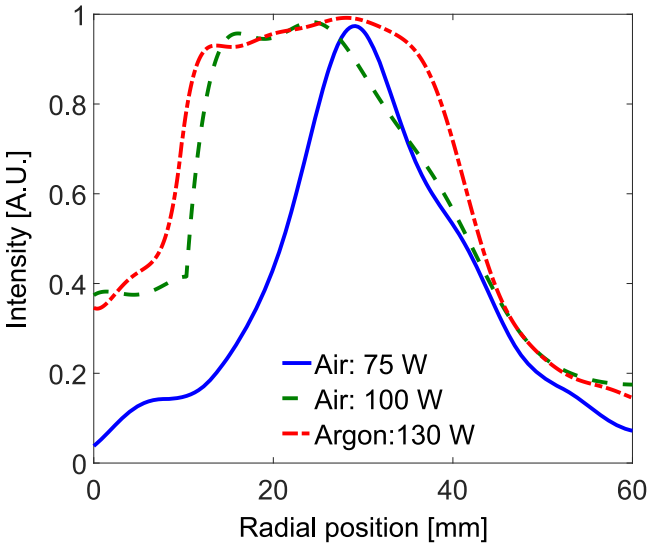

Figure 20. Radial profile of electron density obtained by space resolved x-ray spectroscopy.

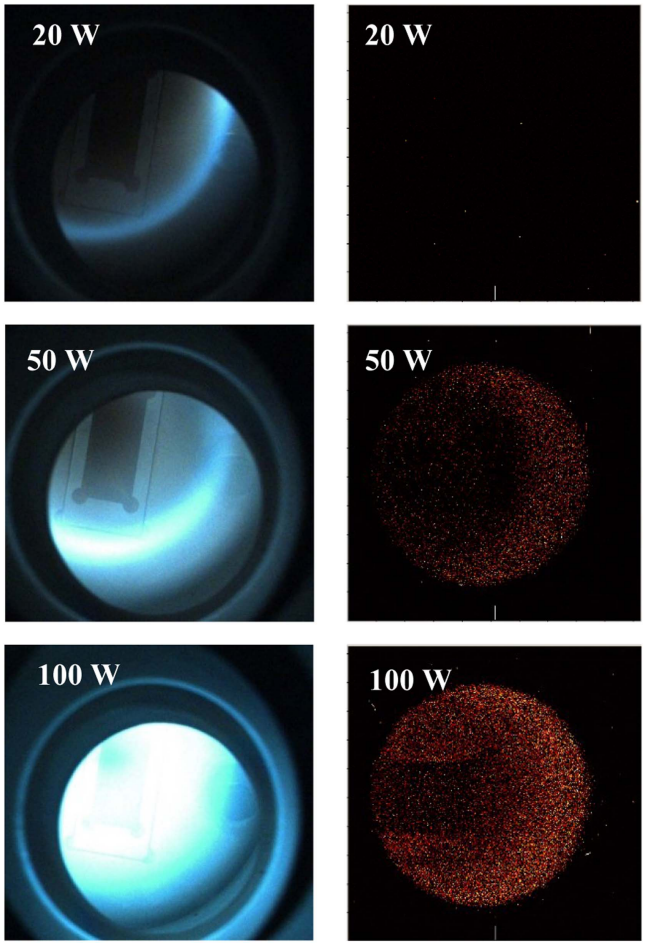

Figure 19. On the left, imaging in optical domain, on the right imaging in the x-ray domain.

cases, imaging techniques were applied using CCD cameras. In the case of x-ray imaging, space resolved spectroscopy was possible, by operating in the above-mentioned PCM. A second, routine CCD camera for optical inspection was placed in the same position as the x-ray pinhole camera, thus providing images for direct comparison. The images shown in figure 19 present evidence that the plasma structure, too, depends on the power level. At 20 W, the plasma appears as a thin ring; no x-ray radiation is emitted, in accord with the results discussed in section 3.1. Above the 48 W threshold, the ring in the visible domain becomes more intense and a slight x-ray emission occurs; the shape of the plasma region emitting x-rays is the same as the emission region in the visible range. Above 80 W, the shape of the plasma is suddenly modified: a very bright annulus appears at optical inspection, with a darker 'hole' inside; the same structure is evident in the x-ray domain imaging. This characteristic plasma shape resembles very closely that observed and characterized by Nagaoka [18]. Figure 20 shows the radial profile of the x-ray emission in two different emission regimes: 75 W, IIER in air plasma; 100 W (HIER) in air plasma and finally 130 W (HIER) in an Argon plasma. The three profiles have been normalized with respect to their maximum value. These profiles illustrate even more clearly than 2D images the dependence of plasma morphology on the pumping wave power.

At 75 W, the x-ray distribution is peaked at 30 mm from the plasma chamber axis and the layer is $\sim 4-5$ mm width (blue line). When overcoming the second power threshold, the layer enlarges up to 10–15 mm, assuming the plasma hole shape (green line). The red line shows the radial distribution of an argon plasma at 130 W. In such a case, the plasma has a main radial width up to 30 mm. This implies that, although the characteristics of the x ray emission do not change with the gas-type, as exhibited in figure 11, the plasma structure depends on the gas specie as well as on the RF power level.

3.5. Discussion and modelling

The results shown in the previous sections provide the combination of radial (obtained by x-ray imaging) and axial

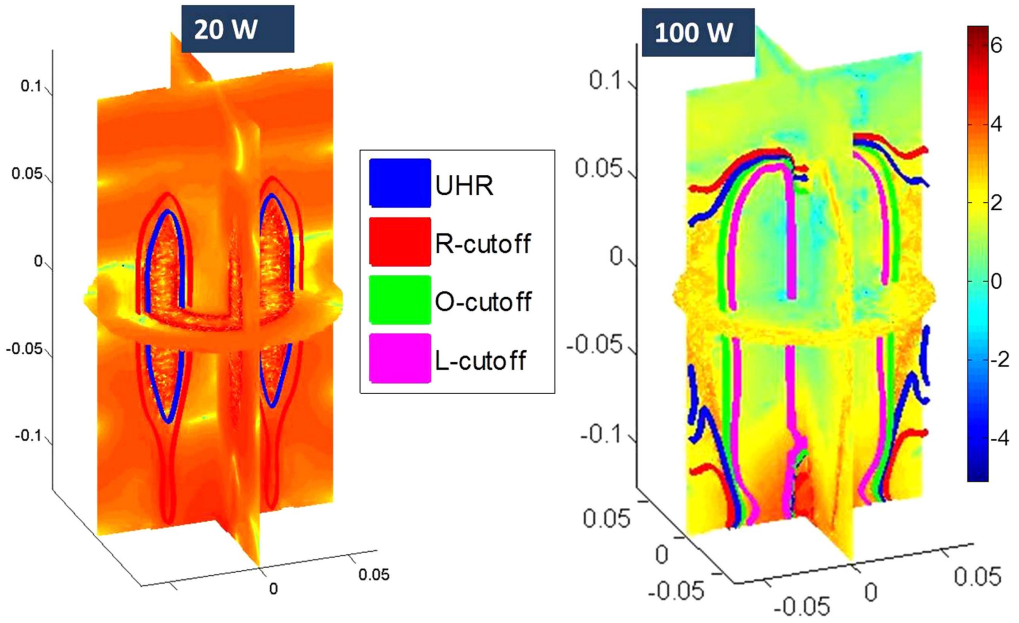

Figure 21. Comsol simulation of EM field distribution in the plasma reactor in presence of plasma. On the left: the results obtained at 20 W RF power. On the right: the results at 100 RF power. UHR, R, O and L cut-off are also shown.

(along the LP penetration axis) plasma density profiles. Thus, a rough 3D structure of the whole plasma within the chamber can be figured out, and used as input for full-wave simulations of the wave-plasma interaction.

We assumed that plasma has cylindrical symmetry, and in cylindrical coordinates could be described by means of the following expression:

$$n(z, r) \cong n(z)n(r)$$

neglecting any dependence on the azimuthal coordinate. We estimated $n(r)$ from the x-ray radial profile, assuming that it is representative of the radial profile of the whole plasma. This hypothesis is reasonable since the structures in the optical and x-ray domain correspond each other, as shown in the previous section. Furthermore, the LP penetration axis collected profile was considered as the longitudinal density profile $n(z)$. This last assumption is affected by some minor sources of errors, for at least two reasons: (i) the LP penetration axis forms an angle of 14° with respect to the plasma chamber axis; (ii) the LP penetration into the chamber modifies the chamber's electromagnetic properties, thus perturbing the actual distribution of the density. However, the assumptions made allow obtaining a first, rough estimation of the overall plasma distribution that is very useful for arguing the wave-plasma interaction in a full-wave approach.

We used the Comsol multiphysics suite [38], following the approach described in [39, 40].

Figure 21 shows the results of the simulation. The false color scale (from blue to red) represents the intensity of the EM electric field within the chamber (units in the colorbar are given as powers of 10), while the 'ribbon-like' lines represent the displacement of resonances and cut-offs.

The left of figure 21 shows that at 20 W the UHR alone occurs in the plasma, embedded by the R cut-off layer. This configuration is compatible with plasma generation supported by direct absorption of the wave at the UHR, following a heating mechanism already described in [22].

At 100 W, R, O and L cut-offs also coexist, in addition to the UHR. In the proximity of the cyclotron harmonics, the UHR is surrounded by the R and L cut-offs. These are the mandatory conditions for the establishment of the Budden-type scenario, described in section 2.

The simulation indicates the EM wave cannot penetrate further within the plasma core, being forced to propagate around the overdense region, in the peripheral layers where the density still remains below the highest admitted cut-off, i.e. the L cut-off. This picture has been confirmed experimentally by measuring the EM power within the chamber by means of RF probes (figure 22). Both at 20 W and at 40 W, the EM field penetrates the plasma core, as reproduced by the simulations. However, when overcoming the second power threshold, the EM power drops, according to the simulations.

The simulation results support the hypothesis that a Budden-type scenario is established. To check the validity of this hypothesis the conversion efficiency C_{XB} must be calculated using equations (9)–(10) for the radial density gradient. Since we are not able, currently, to evaluate φ and θ, we have limited our calculation to $|C_{XB}|$.

We estimated the absolute values of the radial density by normalizing the profiles obtained by the x-ray imaging with the data coming from LP diagnostic. In particular, we used the density value when feeding the plasma at 100 W and in proximity of the second cyclotron harmonics, i.e. $X = 3$ (in terms of relative density with respect to the cut-off one). Figure 23 shows the radial density profile (air at 100 W) together with the conversion efficiency (green curve) and the O, R and L cut-off. $|C_{XB}|$ is the maximum one between 40 and 50 mm, i.e. between the L cut-off and UHR, then it drops to zero beyond the R cut-off. These data support the scheme of fast X-EBW conversion, occurring in a Budden-type scenario.

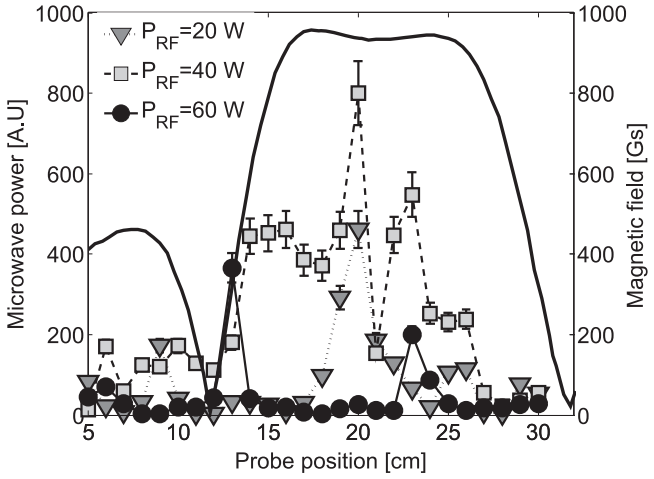

Figure 22. Distribution of the EM power along the LP penetration axis for different values of RF power.

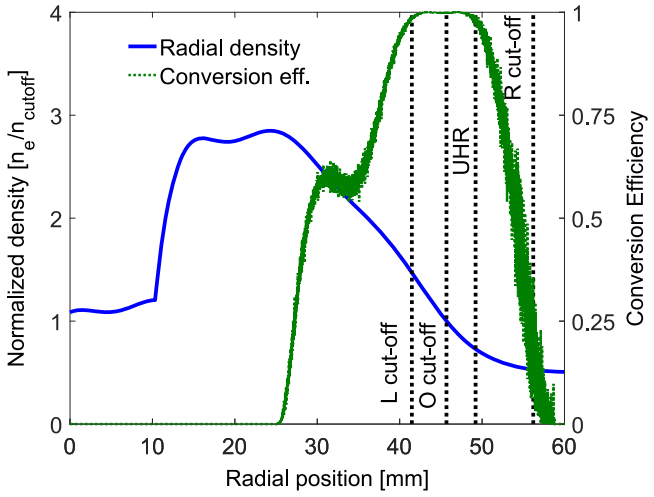

Figure 23. Normalized density and conversion efficiency in the Budden-type scenario versus plasma chamber radius.

The power threshold of 78 W can be explained as the minimum power needed for the establishment of a density-versus-magnetic field reciprocal displacement able to support such a heating mechanism.

3.6. Evidences of collective behaviour

Several experimental evidences indicate that above 78 W the whole plasma (electrons, ions, also including neutrals) starts a fast azimuthal rotation. The most important proof comes from electron energy distribution function (EEDF) measurements, calculated from *I–V* curves collected by the Langmuir probe [41]. EEDF varies in a relevant way according to the LP position. In proximity of the cyclotron harmonics, it assumes the shape shown in figure 24 for P $>$ 78 W. The measured EEDF can be fitted by the superposition of two different Maxwellian curves according to the following equation:

$$F(v) = A_1(t_1) \cdot \mathrm{e}^{-\frac{mv^2}{2t_1}} + A_2(t_2) \cdot \mathrm{e}^{-\frac{m(v-v_o)^2}{2t_1}}. \qquad (13)$$

The term v_0 in the second Maxwellian can be interpreted as

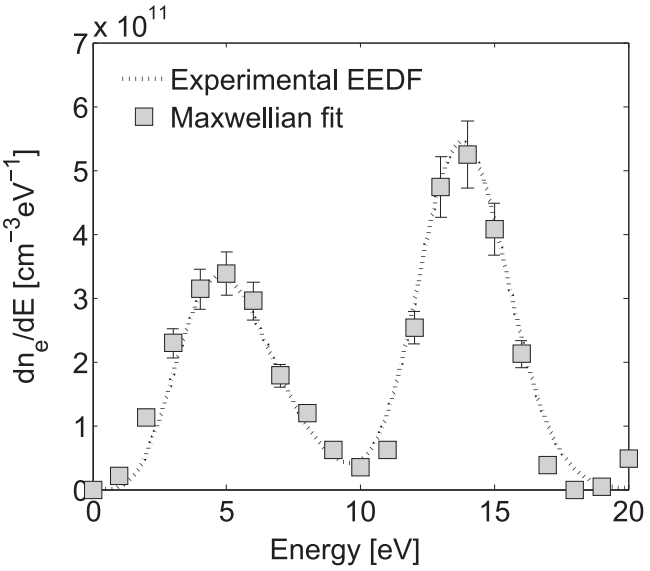

Figure 24. EEDF calculated at the probe position of 13 cm, in proximity of the second ECR harmonic at 3.76 GHz. Two different electron populations are present.

the velocity of the center of mass of an electron population drift with respect to the probe with just that velocity.

The best agreement between experimental and theoretical data has been obtained by considering a relative velocity $v_0 = 1 \cdot 10^5\,\mathrm{m\,s^{-1}}$, corresponding to a kinetic energy of 13 eV.

The rotation of the ion and neutral component has been verified by means of x-ray imaging in photon counting regime [32] when operating in gas mixing mode. In particular, we generated a plasma with a mixture of argon and oxygen. In PCM, we filtered the x-ray emission of the two elements according to their own fluorescence lines (O $\rightarrow$ 0.54 keV, Ar $\rightarrow$ 2.96 keV). The 2D images collected were reduced to 1D plots such as that shown in figure 25, illustrating the distribution of the different species. Ions of the heavier species, i.e. Ar, are placed at larger radii (maximum at 37 mm from the axis). The sum of the two profiles gives a broad radial profile, as shown in the previous section. The displacement between the gases can be easily explained by taking into account the plasma rotation. The centrifugal force, proportional to the mass, could push away argon ions, forcing them to rotate at larger radii. The plasma rotation is accompanied by an interesting effect on the downstream (with respect to the microwave window) neutrals pressure.

Figure 26 shows the neutral pressure for different power. Also in this case, three different emission regimes can be recognized. At P $>$ 78 W the downstream pressure drops by a factor of two. This implies that the plasma collective motion affects also the flux of neutrals out of the plasma. A possible explanation is that plasma rotation could be described by means of a 'typhoon-shaped' plasma vortex, as the one investigated in [14, 15]. This 3D structure is able to transport particles from one side to the other, decreasing the flux of neutrals in one of the two directions.

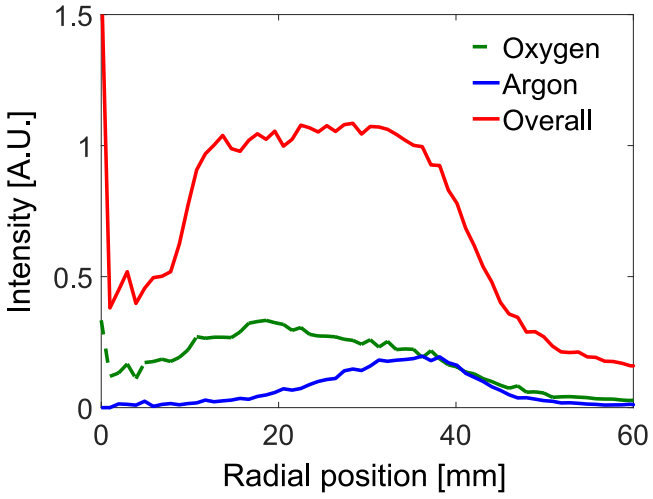

Figure 25. Distribution of argon and oxygen ions versus the plasma chamber radius.

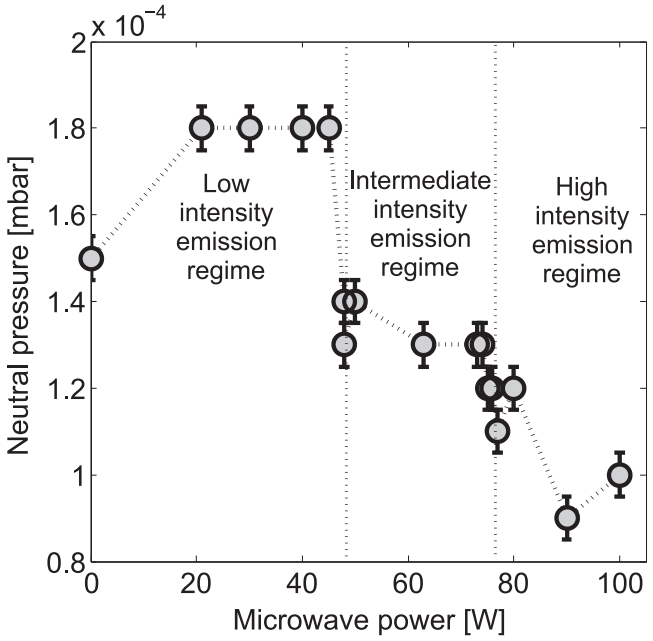

Figure 26. Neutral pressure versus RF power. The pressure drops down above the second power threshold.

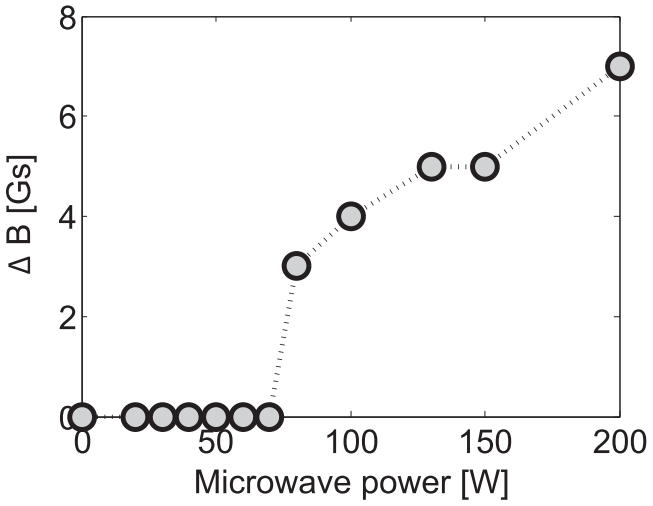

Figure 27. Variation of the axial magnetic field when microwave power is increased. A threshold is visible at 80 W.

This phenomenon has already been observed in other experiments [20], and different explanations can be taken into account:

Nagaoka *et al* [21] propose that azimuthal electron currents are triggered by $\vec{E} \times \vec{B}$ drift due to an electric field (orthogonal to the magnetic field) generated by a steep plasma potential gradient. Furthermore, the radial motion of the particles constituting the plasma hole structure is leaded by a $\vec{F} \times \vec{B}$ drift due to frictional forces. In such a case, the difference of collisionality between the gases (collisionality, in fact, depends on the mass) would imply that argon and oxygen are subject to different $\vec{F} \times \vec{B}$ drift motions, displacing them in different positions.

Golovanivsky [5] hypothesizes that the Sagdeev–Shapiro damping of Bernstein waves leads to an acceleration orthogonal to both magnetic field and the wave propagation direction. In cylindrical symmetry the accelerated electrons form an azimuthal electron current. Finally, Laqua suggests that the mechanism of EBW absorption leads to the generation of an azimuthal current drive [12].

Further investigations are foreseen in future to clarify definitively the nature and the characteristics of the rotating plasma.

Finally, a gauss-meter has been used to detect any plasma self-generated additional magnetic fields; in the case of differential motions of the charged particles, in fact, the azimuthal rotation should generate an axial magnetic field. Figure 27 shows the variation of the axial magnetic field for varying values of RF power. The axial magnetic field increases suddenly at $P > 78$ W. The total current density, due to the contribution of ions and electrons, is:

$$\vec{j} = q_e n_e \vec{v}_e - q_i n_i \vec{v}_i = q_{e,i} n_{e,i} (\vec{v}_e - \vec{v}_i). \qquad (14)$$

Assuming $q_e n_e = q_i n_i$ because of the plasma quasi-neutrality. Therefore, the variation of the axial magnetic field implies that the electron and ion fluid rotate with different velocities. $\vec{E}x\vec{B}$ drift could be invoked as possible mechanism driving the plasma rotation. Equation (12) enables to estimate the needed electric field. Considering $B = 0.07$ T (the applied magnetostatic field induction at second harmonic) and the drift electron energy such as $W^{max} = 13$ eV, it comes out (equation (12)) that $|\vec{E}| \sim 1.5 \cdot 10^3$ V cm^{-1}, a value comparable to that found in [21].

We are not able, currently, to say whether the rotation momentum is transferred to ions and neutrals by electrons through electron–ion and electron–neutral collisions, or if the positive ions are also driven by $\vec{E}x\vec{B}$ drift. It could be argued that ions are only slightly magnetized because of the high collision frequency and thus $\vec{E}x\vec{B}$ drift would not act on them. On the other hand, momentum transfer from electrons to ions requires times of the order of several ms for acquiring energy from electrons, higher than the usual confinement time

expected for these kind of magnetic field structures, lying in the range of a few hundred μs.

4. Conclusions and perspectives

The studies carried out at INFN-LNS permitted characterization of an overdense plasma in an off-ECR heating configuration.

The non-linear behaviour of the plasma energy content (density and temperature product) has been explained in terms of different regimes, the last of which being activated by the fast X-B mode conversion mechanism in a Budden-type scenario. The plasma characteristics at different power levels have been classified in terms of x-ray emission fluxes. In particular:

- **LIER** (low emission) was obtained at the lowest RF power when the plasma looks like a bright ring with negligible x-ray emission and stays below the density cut-off.
- **IIER** (intermediate emission) is generated (at $1.5 \cdot 10^{-4}$ mbar) above a first power threshold around 48 W; plasma maintains its ring-like shape as in LIER, but x-ray emission is strongly increased and photons up to 15 keV are observed. Wave spectrum is characterized by low frequency signal also, in the range 7–15 kHz.

HIER (strong emission) was generated above a second power threshold of 78 W in the same pressure range. Plasma becomes even 3–4 times overdense, emitting x-ray photons above 30 keV. In the wave spectrum, the low frequency signals shift in the 200–300 kHz, or even MHz range. The plasma structure is modified into a plasma hole, a structure apparent in both visible and x-ray domains. Some signatures of fast plasma rotations are also evident. HIER seems to be generated by fast X-EBW conversion in the Budden-type scenario. The overall experimental results cannot be explained by taking into account exclusively the direct absorption of the wave at second harmonic or UHR; in fact, any eventual heating due to second harmonic absorption should manifest a monotonic, smooth increase of the electron temperature versus the input power. Detailed calculations were done by, among others, Girard *et al* in [42]. They found a scaling of the average electron energy, which may explain the well known saturation of the plasma energy content when heated by direct first/second harmonic ECR. However, it is possible that UHR or second harmonic heating could play a role in low energy emission regime and in the few microseconds or milliseconds of plasma life. In fact, EBW requires the upper hybrid resonance layer (and therefore a plasma) already to exist somewhere to trigger EM to EBW conversion.

The increase of electron density and the generation of an overdense plasma could represent a key step for the overcoming of the limitation of modern ECRIS, since it immediately leads to an increase of the extracted current $I_{\text{extr.}}$:

$$I_{\text{extr.}} \propto n_{\text{e}}$$

However, the probable detrimental effects due to the ion heating induced by the ion waves excited during the EBW excitation must be taken into account.

The increase of the ion temperature T_{i} can act in two different ways, both negative:

1. **Increase of the beam emittance**: The normalized beam emittance ε is proportional to $T_{\text{i}}{}^{1/2}$, so any increase of ion temperature makes the beam emittance worse. Evidences of connections between EBW and emittance increase have been published in [9, 43]
2. **Decrease of ion lifetime**: ion lifetime is propotional to $T_{\text{i}}^{-5/2}$ due to diffusion effects. Therefore, the increase of the ion temperature could also lead to a worsening of ion lifetime, and could make the generation of highly charged ions—which require the longest confinement times—more and more difficult.

The quality parameter allowing comparison of the benefits due to the increase of extracted current with the limitations induced by ion heating is the brightness B_{n}, defined as the ratio between extracted current and emittance [1]:

$$B_n = \frac{2I_{\text{extr.}}}{\pi^2 \varepsilon^2}.$$

If the EBW heating mechanism enables increasing the beam current more than beam emittance, then brightness increases. The comparison between brightness measured with different heating mechanisms (ECR and EBW heating) shall tell us if EBW heating can be considered as a step forward for ion sources.

Anyway, these studies have large relevance for basic plasma physics, since they improve our knowledge about electron and ion energy distribution functions, and factors which can lead to its modification or lead to the arise of ion instability.

In future, the proper set-up to continue the investigation on EBW heating will be the flexible plasma trap, fully operational for some weeks at INFN-LNS. The flexible plasma trap is characterized by a flexible magnetic field, generated by three solenoids that allow the tuning of the magnetic field profile. The fine tuning of the magnetic field will make possible the investigation of magnetic configurations that could not be studied on the plasma reactor because of the rigidity of its magnetic field. Different heating schemes, such as the O-Slow X-EBW conversion, should be available in the new test bench, and EBW generation will be studied over a larger range of electron densities and temperature. Plasma generated by flexible plasma trap will be studied by means of diagnostics placed parallel and perpendicularly to the magnetic field symmetry axis.

Acknowledgments

The support of the 5th National Committee of INFN through the RDH-UTOPIA experiment is gratefully acknowledged. The contribution of L Allegra, S Passerello and F Chines has been essential for the present work.

References

[1] Geller R 1996 *Electron Cyclotron Resonance Ion Sources and ECR Plasmas* (Bristol: Institute of Physics Publishing)
[2] Gammino S *et al* 2009 *Plasma Sources Sci. Technol.* **18** 045016
[3] Gammino S 1996 *Rev. Sci. Instrum.* **67** 12
[4] Bernstein I B 1958 *Phys. Rev. Lett.* **109** 10
[5] Golovanivsky K S, Dougar-Jabon V D and Reznikov D V 1995 *Phys. Rev.* E **52** 2969
[6] Podoba Y Y, Laqua H P, Warr G B, Schubert M, Otte M, Marsen S and Wagner F 2007 *Phys. Rev. Lett.* **98** 255003
[7] Preinhaelter J *et al* 2009 *Plasma Phys. Control. Fusion* **51** 125008
[8] Mascali D, Celona L, Gammino S, Miracoli R, Castro G, Gambino N and Ciavola G 2011 *Nucl. Instrum. Methods* A **653** 11
[9] Castro G *et al* 2012 *Rev. Sci. Instrum.* **83** 02B501
[10] Preinhaelter J and Kopecký V 1973 *J. Plasma Phys.* **10** 1
[11] Chen F F *Introduction to Plasma Physics* pp 242–78
[12] Laqua H P 2007 *Plasma Phys. Control. Fusion* **49** R1
[13] McDermott F S *et al* 1982 *Phys. Fluids* **25** 1488
[14] Wilhelm R *et al* 1984 *Plasma Phys. Control. Fusion* **26** 143
[15] Jones B *et al* 2003 *Phys. Rev. Lett.* **90** 165001
[16] Shiraiwa S *et al* 2006 *Phys. Rev. Lett.* **96** 185003
[17] Ono M *et al* 1999 *Proc. 17th Int. Atomic Energy Agency Fusion Energy Conf.* vol 3 (Vienna: IAEA) p 1135
[18] Ram A K, Bers A and Lashmore-Davies C N 2000 *Phys. Plasmas* **7** 4084
[19] Budden K 1985 *The Propagation of Radio Waves* (Cambridge: Cambridge University Press) pp 596–602
[20] Sagdeev R Z and Shapiro B D 1973 *Pis'ma Zh. Eksp. Teor. Fiz.* **17** 389
[21] Nagaoka K, Okamoto A, Yoshimura S, Kono M and Tanaka M Y 2002 *Phys. Rev. Lett.* **89** 075001
[22] Popov O, Shapoval S Y and Yoder M D 1992 *Plasma Sources Sci. Techol.* **1** 7
[23] Gammino S *et al* 2010 *Rev. Sci. Instrum.* **81** 02B313
[24] Chen F F, Evans J D and Arnush D 2002 *Phys. Plasmas* **9** 1449
[25] Allen J E, Boyd R L F and Reynold P 1957 *Proc. Phys. Soc.* B **70** 297
[26] Laframboise J G 1966 Theory of spherical and cylindrical langmuir probes in a collisionless, maxwellian plasma at rest *UTIAS Report No.* 100
[27] Chen F F 2001 *Phys. Plasmas* **8** 3029
[28] Chen F F *et al* 2012 *Plasma Sources Sci. Technol.* **21** 055002
[29] Sudit I D and Woods R C 1994 *J. Appl. Phys.* **76** 4488
[30] Chen F F 2009 *Plasma Sources Sci. Technol.* **18** 035012
[31] Andor iKon-M X-Ray Technology User Guide www.tokyoinst.co.jp/product_file/file/AD08_man04_ja.pdf
[32] Mascali D, Romano F P, Altana C, Caliri C, Castro G, Gammino S and Celona L 2D X-ray spectroscopy for overdense plasmas generated in a compact ion source *Plasma Sources Sci. Technol.* in preparation
[33] Mascali D *et al* 2014 *Rev. Sci. Instrum.* **85** 02A956
[34] Ivanov A A and Wiesemann K 2005 *IEEE Trans. on Plasma Sci.* **33** 1743–62
[35] Laqua H P *et al* 1997 *Phys. Rev. Lett.* **89** 3467
[36] Castro G *et al* 2016 *Rev. Sci. Instrum.* **87** 02A507
[37] Grek B and Porkolab M 1973 *Phys. Rev. Let.* **30** 836
[38] RF Module Users Guide COMSOLMultiphysics. 4.3b http://hpc.mtech.edu/comsol/pdf/RF_Module/RFModuleUsersGuide.pdf
[39] Torrisi G *et al* 2014 *J. Electromagn. Waves Appl.* **28** 1085
[40] Mascali D, Torrisi G, Neri L, Sorbello G, Castro G, Celona L and Gammino S 2015 *Eur. Phys. J.* D **69** 27
[41] Chakravarti P K *et al* 1977 *Rev. Sci. Instrum.* **48** 1344
[42] Girard A *et al* 2000 *Phys. Rev.* E **62** 1182
[43] Miracoli R *et al* 2012 *Rev. Sci. Instrum.* **83** 02A305